ADVANCED MATERIALS INTERFACES
Open Access
www.advmatinterfaces.de

# Ligand-Binding Mediated Gradual Ionic Transport in Nanopores

*H. Samet Varol, Claire Förster, and Annette Andrieu-Brunsen**

**Selective binding of metal ions to their receptors at the cell membranes is essential for immune reactions, signaling, and opening/closing of the ion channels. Such ligand-binding-based pore activities inspire scientists to build metal-ion-responsive mesoporous films that can interact with metal ions to tune the ionic nanopore transport. However, to apply these mesoporous films in novel sensing and separation applications, their ligand-binding-triggered ionic pore transport needs to be understood fundamentally toward programming the transport of both anions and cations simultaneously and gradually. Herein, it is shown how $Ca^{2+}$ ion concentration and attachment to the different chemistry silica nanopores tunes finely the nanopore transport of both anions and cations, especially for phosphate-containing polyelectrolyte (PMEP) functionalized mesopores. This biased ligand binding can gradually regulate the transport of anions and cations, whereas pores without polymers can gradually regulate only the anionic transport. Last, pore polymer functionality related to $Ca^{2+}$ ion binding also diverts the pores' adsorption/desorption (reversibility) response. Almost fully reversible $Ca^{2+}$ binding is observed in non-functional pores and non-reversible $Ca^{2+}$ binding at the PMEP-modified pores. It is also demonstrated that non/functional pores, even at sub-µM concentrations, bind only divalent $Ca^{2+}$ ions, but they are not selective to trivalent $Al^{3+}$ ions.**

## 1. Introduction

The binding of $Ca^{2+}$ ions to its receptors to regulate the ionic current inside the natural ion channels is essential for many biological functions, such as controlling the nervous system and muscular contraction.[1–4] This critical role of $Ca^{2+}$ ion binding in complex biological systems inspired scientists to design $Ca^{2+}$ ion-binding ion channels, such as hybrid mesoporous films changing their ionic pore transport via $Ca^{2+}$ binding at their pores.[2,5–7] In 2012, Brunsen et al. showed phosphate bearing polyelectrolyte—namely poly-(2-(methacryloyloxy)ethyl phosphate (*PMEP*)—inside silica nanopores to regulate the transport of anions between "on (transported)"/"off (rejected)" states via $Ca^{2+}$ ion binding to these functional pores at relatively high $Ca^{2+}$ concentration.[6] They also used similar PMEP-functional pores to bind $Mg^{2+}$ as another divalent cation influencing the nanopore transport under alkaline conditions; however, they did not investigate the capability of these walls to interact with other metal ions with multi-valency such as $Al^{3+}$.[6] Toward considering the presented mesoporous films for advanced material interface applications such as industrial water treatment and reuse,[8,9] or ionic sensing,[10] it is also crucial to investigate the ionic selectivity of the nanopores against other metal ions with different valency. As another $Ca^{2+}$-ion binding controlled nanopore transport work, Ali and co-workers functionalized a single conical nanochannel with a length of 12 µm with molecular phosphonic acid groups to investigate pH-dependent $Ca^{2+}$ ion binding to the pores to vary the ionic current rectification behavior.[5] Their work also covered the relation between $Ca^{2+}$ concentration (range between 10 µM and 1 mM) and gradual monovalent cation but not on anion transport. Recently, Li et al. showed the importance of binding $Ca^{2+}$ ions to a single polymeric nanochannel functionalized by phosphorylated peptide for inactivating ("off" state) the ion flow in neutral conditions.[11] Similar to the single pore polyethyleneterephthalate (PET) film used in the work of Ali et al.,[5] Li et al. also used a thick film (12 µm) with the smallest opening of 40 nm, which is a limited pore opening to select finely the hydrated ions.[11] Their nanochannel is also eligible to control the ionic transport at "on" and "off" states but does not offer a gradual ionic transport control. Therefore, to apply ligand-binding triggered nanopore transport in applications such as ionic separation and electrodialysis, it is still required to have a new multipore (high surface area) thin film system with a small pore size in the range of hydrated radius of ions, as well as to control the transport of both cations and anions gradually beyond "on" and "off" selectivity.

Using stimuli-responsive polymers inside the nanopores has received very high interest in nanotechnology during the last 15 years.[12,13] Thanks to their versatile, tailor-made chemistry,

H. S. Varol, C. Förster, A. Andrieu-Brunsen
Ernst-Berl Institut für Technische und Makromolekulare Chemie
Technische Universität Darmstadt
64287 Darmstadt, Germany
E-mail: annette.andrieu-brunsen@tu-darmstadt.de

The ORCID identification number(s) for the author(s) of this article can be found under https://doi.org/10.1002/admi.202201902.



**DOI: 10.1002/admi.202201902**

and stimuli-responsive nature, polymers provide an extensive library of multifunctionality to the nanopores.[6,14–17] Recent technology proposes tuning ionic nanopore transport by grafting polyelectrolytes at their pore sites.[13,18,19] Polyelectrolytes are appealing for programming the ionic nanopore transport based on the i) possibility of binding ions to themselves (ion- or ligand-binding),[5,6,13,20] ii) ability to vary the wettability of the membrane surface as well as the nanopores,[13,21,22] and also iii) possibilities to change the charge density in the pore sites gradually.[23,24] However, literature still seeks experimental studies explaining the role of polyelectrolyte absence/presence on the ligand-binding in confined space. Theoretical literature in recent years focused on explaining how polyelectrolyte functionalization in nanoconfinement (e.g., inside nanopores or around nanoparticles) affects the binding equilibrium between ligand and receptors.[25,26] For instance, Lopez and Nap introduced a new molecular theory to study the changes in the conductance of a nanopore coated by polyelectrolytes that can bind multivalent counterions such as calcium to themselves.[27] They showed theoretically that the ionic current inside the nanopore could be controlled by the calcium concentration and the environmental pH. In terms of experimental works to date, $Ca^{2+}$ ion (also $Mg^{2+}$) binding to polyelectrolyte functional pores has been studied at high pH[6] and low pH[7] conditions to provide anionic transport at gating stages between "on" or "off" states. To go beyond on/off state pore accessibility (gating), gradually adjusted or finely tuned nanopore ionic transport has been a target for the nanopore community in recent years.[12] Various synthetic strategies have been successfully applied in polyelectrolyte functional nanopores to make them accessible to ions in a gradual way. For instance, our group has proposed a method to gradually change the pH at the pores to vary the charge of PDMAEMA-b-PMEP block-*co*-oligomers at the pore sites to select both cations and anions at the same functional pores just as a factor of environmental pH.[7] Besides, varying the amount, grafting density, and chain length of the polyelectrolytes at the pores are well-known strategies to code the charge density at pore sites to affect ionic pore transport gradually.[12,13,19] Rather than changing the solution pH and nanopore chemistry, simply binding metal ions ($Ca^{2+}$) at the charged nanopores and slowly varying their electrostatic repulsion/attraction between pore walls and ionic probes would be used to tune the ionic nanopore selectivity gradually. Previously, Ali et al. showed $Ca^{2+}$ ion binding reversibility and very low-level (10 μM) $Ca^{2+}$ detection sensitivity from the phosphate-bearing polymer functionalized single nanopore ion-track etched membranes.[5] Alternatively, as mentioned previously, the only one-directional (binding) mechanism of the $Ca^{2+}$ ions to the multi-pore mesoporous silica films having smaller diameter pores (at the range of hydrated ions) was discussed.[6,7] However, the $Ca^{2+}$ binding reversibility and sensitivity to low concentration $Ca^{2+}$ ion-binding (<1 μM) of the PMEP functional pores in this literature were not investigated yet, and these pore activities are exciting for novel nanopore technologies, especially for different sensing applications. For instance, it is still a challenge for sensor technologies to design a metal ion sensor detecting only certain valency number ions even at sub-μM concentrations, and in the end, reporting—or memorizing—only the highest (peak value) concentration of metal ion of a solution with constantly changing metal ions concentration in time.

To date, literature on $Ca^{2+}$ ion-binding triggered ionic nanopore transport has remained limited to control mainly the transport of only a single type of ion (mainly anions) and between "on" and "off" states of the ionic transport at multiporous systems. This study proposes using $Ca^{2+}$ ion binding to gradually tune the transport of cations and anions through silica nanopores with and without polyelectrolytes (PMEP) inside at a fixed pH and fixed pore chemistry/functionalization. The nature of obtaining different gradual ionic transport in our different chemistry mesopores has been described in terms of Langmuir adsorption isotherms fitted to our experimental data. Langmuir isotherms and cyclic voltammetry (CV) curve analysis results show a larger affinity between the $Ca^{2+}$ ions and PMEP-functional pores, which is the fundamental reason for obtaining such nanopore transport for both ions in the PMEP-functional pores as compared to silica mesopores. Langmuir adsorption constants also showed us that anionic transport is more sensitive to $Ca^{2+}$-ion binding than cationic transport. Thus, silica nanopores without PMEP with limited affinity could only control the transportation of anions but not of cations. $Ca^{2+}$ ions could only be fully adsorbed/desorbed (reversibility) in the non-polyelectrolyte-containing pores. More vital electrostatic interaction between $Ca^{2+}$ ions and negatively charged phosphate groups of the PMEP creates a stronger binding of $Ca^{2+}$ ions; and thus, poor adsorption/desorption reversibility. Thereby, the functionalized mesopores only selectively bind $Ca^{2+}$ ions but not trivalent $Al^{3+}$ ions. Our work offers metal ion binding at nanopores as a new method to regulate ionic nanopore transport gradually, reversibly, selectively, and susceptibly at <1 μM concentration toward designing next-generation ion-selective mesoporous membranes and sensors.

## 2. Results and Discussion

### 2.1. Production of Mesoporous Films With and Without Polymer (PMEP) Functionalization

To investigate ligand binding in phosphate-bearing polymer functionalized mesopores, we functionalized the pores of multipore mesoporous silica films by PMEP (**Figure 1**a). First, all the mesoporous silica films were deposited on indium tin oxide (ITO)/glass substrates via dip-coating and evaporation induced self assembly.[28] As deduced from ellipsometry (Figure 1c) and trans-electron microscopy (TEM) (Figure S1, Supporting Information,) the mesoporous silica films have a free pore volume of ≈45 vol%, thickness in the range of ≈180 nm. These numbers are in a good agreement with literature showing similar dip-coated films,[7] and indicating that the films consist of nanopores with 6–7 nm diameter, neck diameters of 3 nm, and ≈440 $m^2\ g^{-1}$ specific surface area.[29,30] For pore functionalization, silica films were first immersed inside a photoiniferter (*N,N*-(diethylamino) dithiocarbamoylbenzyl (trimethoxy)silane) (SBDC)) solution for grafting SBDC at the surface silanol groups on the mesoporous silica films (Figure 1) in accordance to a previously published protocol.[7,29–30] After SBDC grafting, the films were treated with

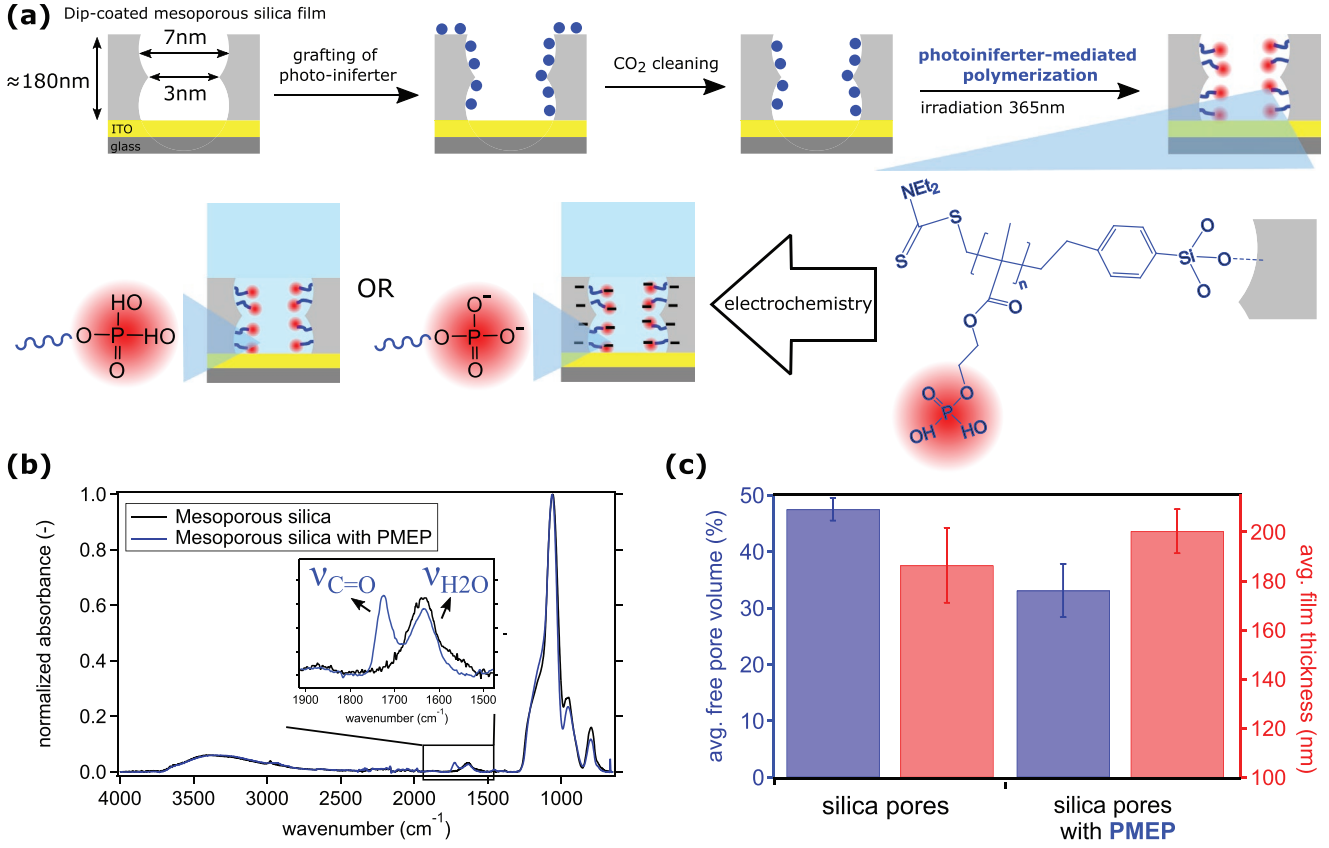


**Figure 1.** a) Graphical illustration presenting our mesoporous films and how to functionalize their pores by poly (2-(methacryloyloxy)ethyl phosphate (PMEP). PMEP at the pores gets positively charged or remains non-charged when the pores are in contact with the alkaline (pH = 10) or acidic (pH = 3) electrolyte, respectively. b) Normalized (at 1065 $cm^{-1}$ from the Si—O—Si vibration) ATR-IR spectra of silica films with (blue) and without (black) PMEP at their pores. Inset magnifies a portion of the fingerprint region, presenting the characteristic $\nu_{C=O}$ and $\nu_{H2O}$ vibrations originating from the pore functionalization, and absorbed water molecules to the silica film, respectively. c) Ellipsometry results presenting the average pore volume (blue-left axis) and average film thickness (red-right axis) as a factor of PMEP functionalization. Error bars are sd.

$CO_2$ plasma to remove the grafted SBDC from the outer film surface to obtain grafted SBDC only within the pores. Then, samples were immersed into monomer (2-(methacryloyloxy)ethyl phosphate (MEP) solution and photopolymerized. Upon PMEP mesopore functionalization, ATR-IR spectra shows a new vibrational band at 1730 $cm^{-1}$ originating from stretching vibration from the C=O ($\nu_{C=O}$) groups of PMEP (Figure 1a).[31] We also measured ATR-IR spectra of the PMEP functional films without the $CO_2$-plasma cleaning step (Figure S2, Supporting Information) and showed stronger peak intensities of the characteristic PMEP vibrations due to additional polymer on the film surface. After $CO_2$-plasma cleaning and subsequent PMEP pore functionalization, we detected a decrease in the free pore volume (blue bars in Figure 1c) while not observing a change in the film thickness (red bars in Figure 1c). Ellipsometry results also agree with the IR findings that the detected C=O vibration originates from the presence of PMEP at the pore sites but not on the film surface. As presented in Figure 1a, the phosphate groups of PMEP are expected to be deprotonated at alkaline conditions ($MEP^{2-}$, pH = 10), which are expected to result in an attraction of $Ca^{2+}$ ions and pore wall neutralization via chelation; thus, changing the ionic pore transport.[6,32,33]

### 2.2. Gradual Transport of Ions by $Ca^{2+}$ Addition (Ligand-Binding)

By using CV, we studied the relation between $Ca^{2+}$ ion binding and the transport of anionic ($[Fe(CN)_6]^{3-/4-}$) and cationic ($[Ru(NH_3)_6]^{2+/3+}$) redox probes at our nanopores without (**Figures 2**a,c) and with PMEP functionalization (Figures 2b,d). Previous works have shown the effect of $Ca^{2+}$ ion-binding on the transport of only anionic redox probes at alkaline or changing pH conditions through pH-responsive polymer functionalized pores.[6,7] For instance, the work of Ali et al. showed that the gradual binding of $Ca^{2+}$ ions at 12 µM long conical shape pores creates a change in the transport of cations ($K^+$), especially between the concentration of 0 and 10 µM (85% change in the detected voltage).[5] Here, we focus on ligand-binding originated gradual transport control of both anions and cations as well as on varying $Ca^{2+}$ ion concentration in a wide range between 0 and 5 mM. Small nanopores of our mesoporous films allowed us to detect differences in both cation and anion transport via $Ca^{2+}$ binding more sensitively even at high $Ca^{2+}$ loadings compared to the changes detected in literature.[5,6,7] We quantify these changes in the next section in details. To deprotonate the mesopores of both silica films, with

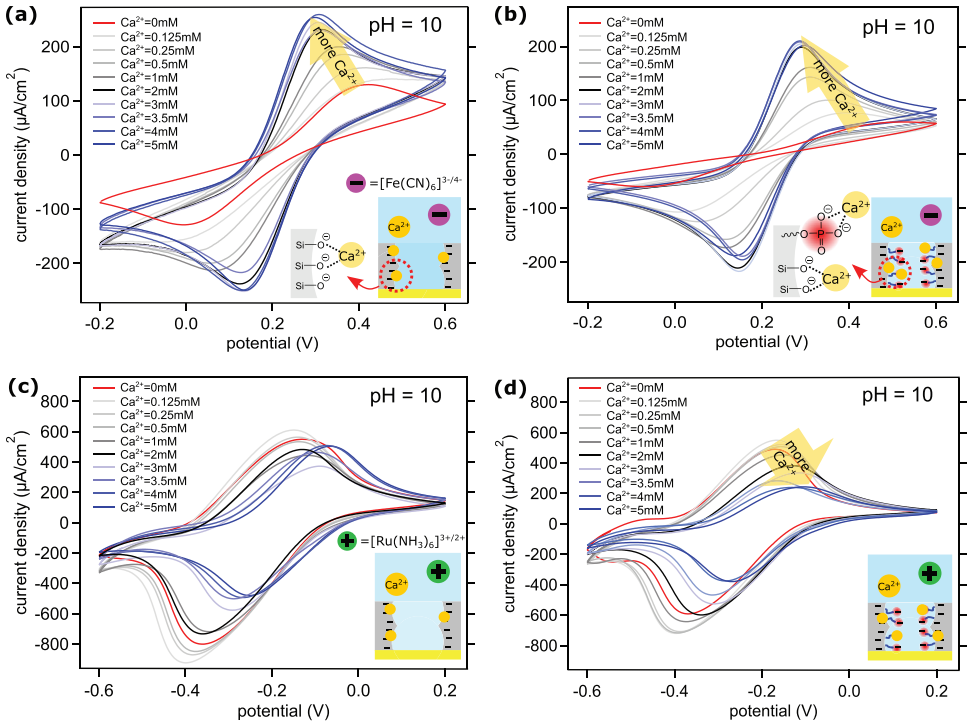


**Figure 2.** Cyclic voltammograms of mesoporous silica films a,c) before and b,d) after their PMEP pore modification. All measurements performed at a fixed pH value of 10 but with different amounts of $Ca^{2+}$ ions inside the electrolyte solutions. $[Fe(CN)_6]^{3-/4-}$ (a,b) and $[Ru(NH_3)_6]^{2+/3+}$ (c,d) were used as anionic and cationic redox probes, respectively. The scan rate used for all the measurements was 200 mV $s^{-1}$. Insets illustrate the chemistry of the negatively charged inner pore walls, the electrolytes, and the $Ca^{2+}$ ions in contact with these negatively charged groups.

and without PMEP, or to keep them neutral, we fixed the pH of these solutions at pH = 10 and pH = 3, respectively. We measured the electrolytes with a higher amount of $Ca^{2+}$ ions (>0 mM) after clearly observing that the pores were fully accessible, meaning that the peak current densities from CV measurements reached a plateau (no change in the cyclic voltammograms as a factor of interaction time) (Figures S3 and S11, Supporting Information). All the measurements were performed starting first by measuring CV with the smallest amount of $Ca^{2+}$ concentration (0 mM, red curves in Figure 2) and finishing by measuring the highest (5 mM) amount of $Ca^{2+}$ filled electrolyte (blue curves in Figure 2). At alkaline conditions (pH = 10), both silica nanopores ($Si{-}O^-$) and phosphate groups of PMEP ($MEP^{2-}$), deprotonate (inset of Figure 2). This is in accordance with the literature showing the pKa shift of these groups at nanoconfinement via their deprotonation upon increasing bulk pH.[6,32] The twice negatively charged polyelectrolyte phosphate groups interact with $Ca^{2+}$ ions via chelation, and pore walls gradually get neutralized, as can be deduced semi-quantitatively from Figure 2a,b,d. With increasing $Ca^{2+}$ concentration, a gradual increase in the peak current density is observed as the result of a higher number of anionic redox probes ($[Fe(CN)_6]^{3-/4-}$) diffusing through both non-functional (Figure 2a) and PMEP-functional nanopores (Figure 2b). At acidic pH (pH = 3), both PMEP-functionalized and non-functionalized mesopores are expected to be neutral; thus, the addition of $Ca^{2+}$ did not change the shape of the CV (Figure S4, Supporting Information). At such neutral pores, both anionic and cationic probes could diffuse through the pores and reach the bottom electrode to be detected. Interestingly, increasing $Ca^{2+}$ concentration in PMEP functionalized mesopores gradually reduces the peak current density of cationic ($[Ru(NH_3)_6]^{2+/3+}$) probes (Figure 2d), whereas no systematic change in cationic probe peak current density was detected upon $Ca^{2+}$ addition in the unfunctionalized silica pores without PMEP (Figure 2c). This indicates the polymer-specific interaction with calcium ions. For the positively charged $[Ru(NH_3)_6]^{2+/3+}$ redox probe at basic pH; and thus, when the redox probe and pore wall electrostatically attract each other, increasing $Ca^{2+}$ ion concentration results in narrower CV curves. CV curve broadening in mesoporous silica films with polyelectrolytes at the pore sites has been explained previously due to having an electrostatic interaction between the redox probe and oppositely charged polyelectrolytes.[23] With increasing $Ca^{2+}$ concentration from 0 to 5 mM, both our non-functional (Figure 2c) and functional (Figure 2d) pores become less charged; thus, the electrostatic interaction with the cationic probe $[Ru(NH_3)_6]^{2+/3+}$ and these pore walls seems to be reduced which is reflected in a decreasing peak current density (Figure 2d).

Quantification of $Ca^{2+}$ ion binding triggered gradual ionic transport through our nanopores was done after collecting the maximum peak current densities from CV curves (Figure 2; Figures S4 and S13, Supporting Information) and normalization of these maximum peak current densities (see Supporting Information). Normalized anodic peak current densities ($i_{p,a}$) from the anionic (blue markers) and cationic (red markers) redox probes' transport through the non-functional (**Figure 3**a) and PMEP-functional (Figure 3b) pores at changing $Ca^{2+}$

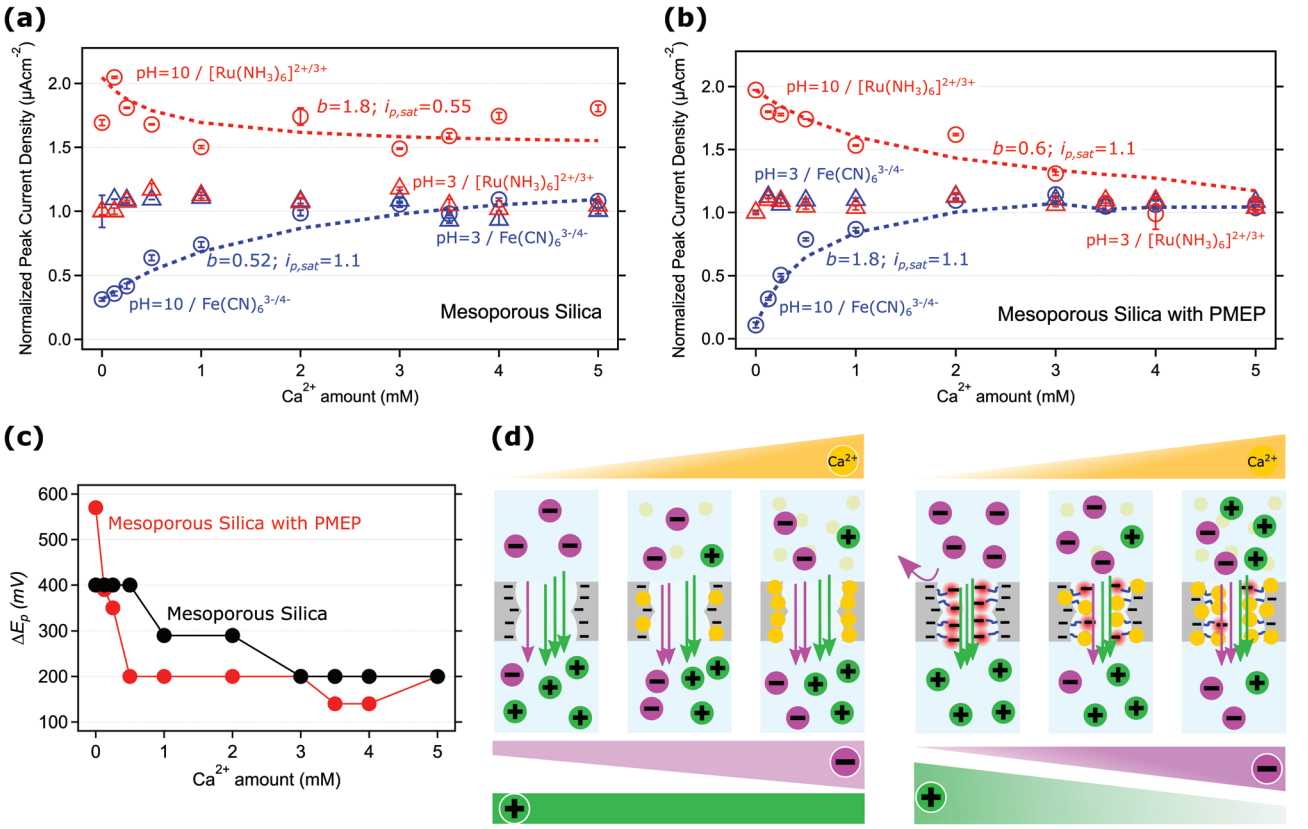


**Figure 3.** Normalized peak current density (μA cm$^{-2}$) of anionic (blue, $[Fe(CN)_6]^{3-/4-}$) and cationic (red, $[Ru(NH_3)_6]^{2+/3+}$) probes as a factor of changing $Ca^{2+}$ amount in the electrolytes in contact with mesoporous silica films a) without and b) with PMEP pore functionalization. Relation between the transport of ions and $Ca^{2+}$ amount was tested at low (triangles, pH = 3) and high (circles, pH = 10) pH conditions. The pH and type of ionic probes were noted next to their data points in (a,b). Error bars are sd. Blue and red dashed lines in (a,b) present the Langmuir adsorption model fit of the normalized $i_{p,a}$ data of $[Fe(CN)_6]^{3-/4-}$ (empty blue circles) and $[Ru(NH_3)_6]^{2+/3+}$ (empty red circles) probe transports at pH = 10, respectively. Dissociation constants (b) and normalized peak current densities where the $Ca^{2+}$ adsorption saturates ($i_{p,sat}$) used to fit the Langmuir isotherms are noted next to each fit. c) Relation between the $Ca^{2+}$ ion amount and the peak-to-peak potential difference ($\Delta E_p$) of the CV curves collected at pH = 10 and using $[Fe(CN)_6]^{3-/4-}$ as the anionic probe. Red and black markers represent the $\Delta E_p$ data of non-pore functionalized and PMEP-functionalized silica films, respectively. d) Illustration of the ionic pore transport mechanism in the nanopores of our films without (left) and with (right) PMEP functionalization at alkaline conditions (pH = 10) and changing amount of $Ca^{2+}$ in the solution (orange triangle bar [top] and orange filled circles). Purple and green bars and filled circles represent the amount of anionic and cationic probes transported through our pores, respectively.

concentrations are presented in Figure 3. Increasing $Ca^{2+}$ ion concentration in contact with the PMEP functionalized nanopores changes the transport of anions between almost entirely rejected (0 mM $Ca^{2+}$) to fully accessible (5 mM $Ca^{2+}$); it also tunes the transport of cations from highly accessible (0 mM $Ca^{2+}$) to less accessible (5 mM $Ca^{2+}$, neutral) transport states (Figure 3b,d). Previous works on nanopores have shown that such a gradual pore transport control of both ions can be possible only by changing the environmental conditions, such as changing the pH[7,34] or changing pore confinement and functionality, for instance, using different chemistry or amount polyelectrolytes.[23,35]

In addition, for the nanopores without PMEP functionalization (Figure 3a, d-left), the anion pore accessibility systematically increased with increasing $Ca^{2+}$ concentration at pH = 10. However, rejection of anions at PMEP-functional pores is more significant than rejection at the non-functional pores when no $Ca^{2+}$ is present in the electrolyte (0 mM $Ca^{2+}$) as the maximum peak current density is not going to zero in case of anion transport in non-functional pores (blue circles in Figure 3a). The interactions between increasing $Ca^{2+}$ ion concentration and negatively charged non-functionalized (dashed line in Figure 3a) and PMEP-functionalized mesopores (dashed lines in Figure 3b), can be described by Langmuir isotherm model fittings. For the anionic probe ($[Fe(CN)_6]^{3-/4-}$), the best fitting parameters were found with Langmuir constants (b) of 0.52 and 1.8 mM of $CaCl_2$ for the non-functionalized and PMEP-functionalized mesopores (blue dashed lines in Figure 3a,b). A higher Langmuir constant from the PMEP functional pores reflects the more specific interaction with $Ca^{2+}$ ions as compared to the affinity between non-functionalized pore silanol groups and $Ca^{2+}$ ions.

In contrast to anion transport, ligand-binding did not play a recurring role in the cation transport in the non-functional silica pores (plateau, empty red circles in Figure 3a) at $Ca^{2+}$ concentrations higher than 1 mM, indicating an equilibrium state is reached between 1 and 5 mM $Ca^{2+}$ ion concentration. Interestingly, at small $Ca^{2+}$ ions concentrations (<1 mM), non-functional silica pores and PMEP functional pores respond similarly against increasing $Ca^{2+}$ concentration with respect to cationic

probe transport regulation at pH = 10 (Figure 3a,b red empty circles). A similar limited response against cationic redox probe transport at alkaline conditions was also detected from the normalized peak current density calculated from the reduction part ($i_{p,c}$) of the CV curves (Figure 2a,c; Figures S4a,c and S7c, Supporting Information) as well as from the CV data of mesoporous films with non-functional mesopores with slight changes in thickness and pore size (mesoporous silica-II in Figure S8, Supporting Information). For cationic probe ($[Ru(NH_3)_6]^{2+/3+}$) CV data in Figure 3b, the best Langmuir isotherm model fittings could be realized by 0.6 mM (PMEP-functional pores) as a constant. For fitting the Langmuir isotherms to the normalized peak current density data presented in Figure 3b (transport at PEMP-functional pores) and for the anionic transport at non-functional pores (blue circles in Figure 3a), we tried to use as much as possible similar fitting parameters for the peak current density level where the ionic transport saturates ($i_{p,sat}$). As seen from the experimental data in Figure 3a,b, all the $i_{p,a}$ values except those obtained from the transport of cations in non-functional pores (red circles in Figure 3a) saturate at $i_{p,a} \approx 1.1$. However, to fit a reasonable Langmuir isotherm to the cationic transport data in non-functional pores (red circles in Figure 3a), we needed to enter a significantly lower $i_{p,sat}$ (0.55) compared to the $i_{p,sat}$, where we could detect from our experimental data which is $\approx i_{p,a} \approx 1.6$. To the best of our knowledge, for a proper Langmuir fit to an experimental data, $i_{p,sat}$ should be close to the $i_{p,sat}$ from the experimental data, similar to our other fittings ($i_{p,sat} \approx 1.1$). Therefore, for the following discussions, we exclude the Langmuir constant ($b$) obtained from the cation transport in non-functional pores and compared only the $b$ obtained from the fittings done by entering similar $i_{p,sat}$.

For the PMEP functionalized mesopores (blue circles in Figure 3b), at ≈2 mM $Ca^{2+}$ ion concentrations, the ionic peak current density ($i_{p,a}$) for the anionic probe ($[Fe(CN)_6]^{3-/4-}$) reaches to the same $i_{p,a}$ from the transport of anions at neutral functional pores (pH = 3 environment, blue triangles in Figure 3b). At the same time, the cationic probe ($[Ru(NH_3)_6]^{2+/3+}$) transport at pH = 10 (red circles in Figure 3b) arrives at the $i_{p,a}$ level from the cation transport detected at pH = 3 solutions (neutral, red triangles in Figure 3b) after addition of ≈4 mM of the $Ca^{2+}$ ions. This difference in calcium ion dependence of anionic and cationic probe diffusion was also detected in our Langmuir isotherms in Figure 3a,b. For mesoporous films with PMEP functionalization, Langmuir constants from the fittings of anionic probes (b = 1.8) are larger than those obtained from the data of cationic probes (b = 0.6). This means that the $Ca^{2+}$ ligand-binding to PMEP has a larger impact on tuning the transport of the anion probe molecule ($[Fe(CN)_6]^{3-/4-}$) which is directly impacted by screening of repulsive electrostatic forces as compared to the cationic probe molecule ($[Ru(NH_3)_6]^{2+/3+}$) which is competing with the $Ca^{2+}$ on PMEP -ion interaction and electrostatic attraction. Regulating the nanopore transport of the applied cationic probes is more difficult by $Ca^{2+}$ binding.

Having the higher $Ca^{2+}$ ion and nanopore affinity when there are PMEP groups inside the nanopore is also demonstrated by the $Ca^{2+}$ concentration dependent changes in the peak-to-peak potential difference, $\Delta E_p$ of the CV curves (Figure 3c). First, all the $\Delta E_p$ values obtained from our CV measurements (Figure 3c; Figure S9, Supporting Information) are larger than 59 mV, indicating strictly reversible single electron transfer at the electrode for our CV measurements.[36,37] At 0 mM $Ca^{2+}$ concentration, there is larger $\Delta E_p$ from the transport data of the anionic probe ($[Fe(CN)_6]^{3-/4-}$) at the PMEP-functional pores than those from the non-functional pores. This indicates less reversible electron transfer at the PMEP functional pores as compared to non-functional ones. However, upon $Ca^{2+}$ ion-binding to both mesoporous films, $\Delta E_p$ for $[Fe(CN)_6]^{3-/4-}$at basic pH is reduced (Figure 3c). This indicates an increased anionic probe transport process reversibility with increasing calcium ion concentration. This indicates a facilitated $[Fe(CN)_6]^{3-/4-}$ transport upon higher $Ca^{2+}$ ion addition in both nanopores probably due to the negative charge at the pore walls being screened by $Ca^{2+}$. Thereby, the $Ca^{2+}$ concentration dependent decrease in $\Delta E_p$ is steeper for PMEP-functionalized mesopores as compared to the non-functional pores. This indicates a stronger charge screening of $Ca^{2+}$ ions in PMEP than in unfunctionalized silica pores walls. If we consider the change $\left(\text{Slope} = \frac{\Delta E_{p,\,1\text{ mM }Ca^{2+}} - \Delta E_{p,\,0\text{ mM }Ca^{2+}}}{\Delta Ca^{2+}\text{concentration (1 mM} - 0\text{ mM)}}\right)$ in $\Delta E_p$ for the $Ca^{2+}$ ion concentration between 0 and 1 mM $Ca^{2+}$ addition as a metric of nanopore detection sensitivity, we find ≈370 mV $mM^{-1}$ and ≈110 mV $mM^{-1}$ as the detection sensitivities for the PMEP-functional and non-functional pores, respectively. Such a high affinity between $Ca^{2+}$ ions and PMEP functionalized pores gradually regulates the transport of cationic and anionic probes.

### 2.3. Reversibility of Ligand-Binding and Ion Detection Sensitivity of the Pores

To study the $Ca^{2+}$ ion adsorption/desorption reversibility as well as the $Ca^{2+}$ ion detection sensitivity of our nanopores without (**Figure 4**a,b,c) and with PMEP (Figure 4b,d), we studied the following $Ca^{2+}$ ion loading and unloading conditions: i) between 0 and 5 mM (Figure 3, red markers) and ii) between 0 and 0.5 μM (Figure 3, blue markers). As mentioned in the previous section, the detection sensitivity of our pores was deduced as, $\text{Slope} = \frac{i_{p,a\,(\text{after }Ca^{2+}\text{ion addition})} - i_{p,a\,(\text{before }Ca^{2+}\text{ion addition})}}{\Delta Ca^{2+}\text{concentration (μm)}}$ from peak current density versus $Ca^{2+}$ ion loading/unloading data before normalization (Figure S12, Supporting Information). Electrolyte solutions were fixed at basic (pH = 10) pH, and we monitored the transport of only anionic ($[Fe(CN)_6]^{3-/4-}$) probes at the pores. Before starting $Ca^{2+}$ ion loading/unloading cycles, the $Ca^{2+}$ ion-free (0 mM) solution was first left in contact with our films until we observed constant peak current densities calculated from the CV curves at increasing liquid/solid contact times (Figures S10 and S11, Supporting Information). The peak current densities at different $Ca^{2+}$ ion loading/unloading scenarios were further processed only after collecting data when the transport of the anions did not change anymore in electrolyte/membrane interaction time (Figures S11 and S12, Supporting Information), and they were normalized to the $i_{p,a}$ collected from the first measurement (0 mM $Ca^{2+}$). In this way, the effect of addition/removal cycles of $Ca^{2+}$ ions at our pores relative to the negatively charged pores that did not contact any $Ca^{2+}$ ions, was compared.

The increase of anionic probe transport as a factor of first $Ca^{2+}$ addition both at high (5 mM) and very low (0.5 μM)

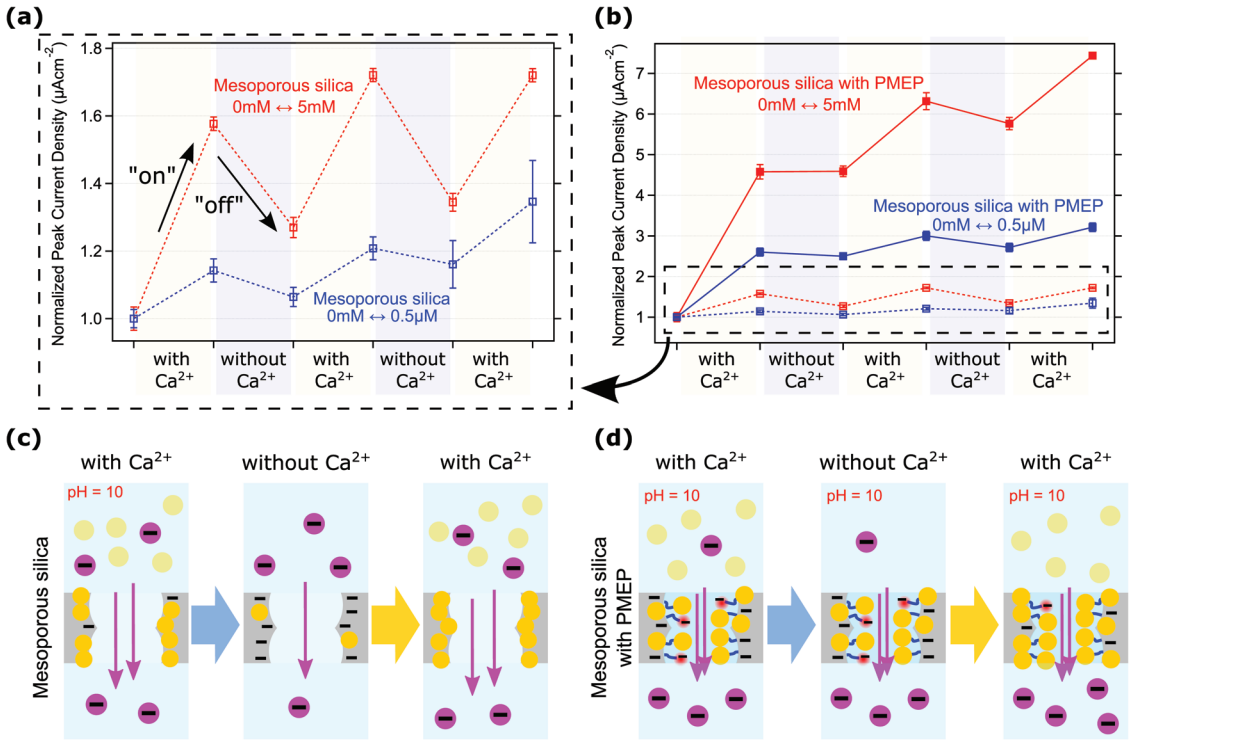


**Figure 4.** Attachment and detachment (called reversibility) mechanism of $Ca^{2+}$ ions at the mesoporous silica pores a) before (empty boxes connected with dashed lines) and b) after (filled boxes connected with straight lines) the PMEP functionalization. Normalized peak current densities from CV curves were collected when we used 5 mM (red), 0.5 μM (blue), or 0 mM $CaCl_2$ solutions as electrolytes (pH = 10). Data inside of the black dashed lined box presents the reversibility of $Ca^{2+}$ adsorption/desorption at mesoporous silica without PMEP. Error bars are sd (a,b). c,d) Variations in the reversibility of $Ca^{2+}$ ion binding in the non-functional (c) and functional pores (d) are illustrated when these pores are filled with $CaCl_2$ containing solutions in the first cycle, then filled by 0 mM $CaCl_2$ solution and, in the end, loaded again with $CaCl_2$ containing solution. $Ca^{2+}$ ions, $[Fe(CN)_6]^{3-/4-}$ probes, and PMEP are sketched by orange-filled circles, purple-filled circles, and blue wavy lines inside the pores, respectively.

concentrations of $Ca^{2+}$ ions are significantly higher for the pores with PMEP functionalization (Figure 4b, straight lines) than those obtained from non-modified pores (Figure 4a,b dashed lines). After the first $Ca^{2+}$ ion loading in the PMEP functional pores (left-orange shaded area, Figure 4a), with respect to the $[Fe(CN)_6]^{3-/4-}$ peak current density detected when there is no $Ca^{2+}$ ion inside of the electrolyte, upon 5 and 0.5 μM $Ca^{2+}$ ion loading in the electrolyte, we detected 360% and 160% increase in the normalized peak current density of $[Fe(CN)_6]^{3-/4-}$, respectively. From these changes, we calculated the $Ca^{2+}$ ion detection sensitivities of our PMEP-functional pores upon 5 and 0.5 μM $Ca^{2+}$ ion loading as ≈0.0126 and 160 μA cm$^{-2}$ μM$^{-1}$, respectively. On the other hand, in the first $Ca^{2+}$ loading cycle, we realized a 60% and 14% increase in the $[Fe(CN)_6]^{3-/4-}$ peak current density for 5 and 0.5 μM $Ca^{2+}$ loaded scenarios inside the non-functional pores, respectively, as compared to the anionic transport detected before $Ca^{2+}$ ion addition (left orange shaded area in Figure 4a). Such more limited changes in the peak current density compared to PMEP-functional pores show less sensitivity for the $Ca^{2+}$ ion detection as 15 and 40 μA cm$^{-2}$ μM$^{-1}$, for the 5 mM and 0.5 μM $Ca^{2+}$ ion loadings. Upon washing the mesoporous films after the first $Ca^{2+}$ ion loading, PMEP functionalized mesopores did not sufficiently release the $Ca^{2+}$ ions bound to the pores (left-blue shaded area in Figure 4a,b). Approximately 0% and ≈4% decrease in the anionic probe molecule peak current density was observed upon the first washing of the PMEP functionalized mesopores filled previously by 5 mM and 0.5 μM $Ca^{2+}$ ions. Differently, the non-functionalized silica mesopores (left-blue shaded areas in Figure 4a) show a strong release of $Ca^{2+}$ ions upon washing the mesoporous films with metal-ion-free electrolyte. Non-functional nanopores filled with 5 mM and 0.5 μM $Ca^{2+}$ ion-containing solutions in the previous step showed a decrease in the anionic peak current density by ≈19% and 7%, respectively, upon washing. This shows a more significant $Ca^{2+}$ ion release from the non-functionalized silica mesopores than the PMEP functionalized mesopores. Furthermore, this $Ca^{2+}$ ion adsorption/desorption behavior showing significant release for the unfunctionalized silica mesopores but only minor release for the PMEP functionalized mesopores, was reproducible for the subsequent adsorption–desorption cycles of non-functional and PMEP functionalized silica mesopores (Figure 4a,b).

Thereby, during the second and third adsorption and desorption cycles by both 5 mM and 0.5 μM $Ca^{2+}$ ion concentrations, a continuous increase in the maximum peak current density of anionic probes was observed with increasing cycles of $Ca^{2+}$ adsorption (middle and right orange shed areas in Figure 4a,b). This increase was more significant for PMEP-functionalized mesopores as compared to unfunctionalized mesopores. However, the increase of anionic transport with increasing $Ca^{2+}$ ion loading at each cycle gets less significant compared to the increase during the first $Ca^{2+}$ ion loading (360% increase

in anion transport) probably indicating slow rearrangement processes of ions and polyelectrolytes inside the nanopores as well as stronger binding of $Ca^{2+}$ to PMEP as to silica pore walls among others related to its physical crosslinking function. Nevertheless, partial removal of the adsorbed $Ca^{2+}$ ions from the PMEP-functionalized pores was achieved by protonating the PMEP at low pH (pH = 3, 0 mM $Ca^{2+}$) (Figure S11b,c, Supporting Information). Even if a complete removal of calcium ions from the PMEP-functionalized mesopores seems not to be possible as the $i_{p,a}$ could not be reduced to those from our first measurement with 0 mM $Ca^{2+}$ solution with pH = 10, we demonstrated that using low pH; and thus, neutralized mesopores is helpful to partly desorb the $Ca^{2+}$ ions from the pores (Figure S11b,c, Supporting Information). Apparently, the PMEP inside the nanopore confinement rearranges irreversibly into a new equilibrium state upon a first contact with calcium ions not being able to recover the initial state under the applied conditions. This shows a *clear memory effect* of such PMEP functionalized mesopores. It must be noted that after partial desorption of the $Ca^{2+}$ ions at acidic conditions (pH = 3) and a very long time of different pH and $Ca^{2+}$ ions containing electrolyte interactions, our PMEP-functional membranes could still respond to calcium ion ligand-binding on the anion transport at pH = 10 (far-right blue and orange shaded areas in Figure S11b,c, Supporting Information).

### 2.4. Valance Number Selectivity of the Nanopores

For potential sensing concepts of metal ions at sub-µM concentrations, cross-influences of other ions are important to consider. To check the valance number selectivity of our pores, we tried to neutralize both non-functional and PMEP-functional pores by using multivalent Al ions (**Figure 5**) as monovalent ions do not seem to disturb our signal as they are constantly present within the supporting electrolyte KCl. Our multivalent Al ion precursor ($AlCl_3$) in water and presence of tiny concentrations of NaOH (see Experimental Section) probably transform into different hydrolyzed aluminum species such as $Al(OH)_4^-$, $AlOH^{2+}$, or $Al(OH)_2^+$ rather than being presented as $Al^{3+}$ at high pH conditions.[38] However, our electrochemical findings demonstrate that both at high pH (Figure 5b) and low pH (where $Al^{3+}$ presents in the solution, Figure S14e, Supporting Information) conditions, multi-valance and hydrolyzed Al species cannot interact with our mesopore systems to influence the ionic transport. However, the normalized peak current densities of cationic probe transport in the PMEP-functional nanopores are higher at all the Al loading levels between 0 and 5 mM compared to those measured from the non-functional pores. Similarly, regardless of adding Al ions to the system, PMEP-functional pores reject more anions than the rejection of the non-functional nanopores. In conclusion, both nanopore systems used in this work selectively bind two-valent ions to themselves but not the trivalent ions. Further proof of our nanopores to be selective only to two-valent ions can be found in previous work of our labs.[6] In that paper, Brunsen et al. used similar PMEP functional nanopores and showed that similar to $Ca^{2+}$-gating, divalent ion, $Mg^{2+}$ can also regulate the nanopore ionic transport.[6] However, they explained that the effectivity of $Mg^{2+}$-binding on the nanopore transport is limited compared to the transport regulated by $Ca^{2+}$-binding. This valency number ionic selectivity of our nanopores can make the proposed mesoporous films to be considered for different applications requiring sensitive detection (or binding) of divalent ions but not of trivalent ones such as biosensors lab-on-chip devices,[39] and electrochemical ionic separation of trivalent metal ions.[40,41]

## 3. Conclusion

We demonstrated that the concentration-dependent interaction of $Ca^{2+}$ ions to the charged and/or PMEP polyelectrolyte functional silica nanopore walls is a powerful tool to gradually tune the ionic nanopore transport at alkaline conditions and can be used as a sensor. Especially, ligand-binding is a potent tool to simultaneously control the transport of both anions and cations at the phosphate-bearing polymer (PMEP) functional silica pores. As supported by the Langmuir adsorption isotherms fitted to our ionic transport data, the better ionic selectivity of PMEP-functional nanopores is probably related to a stronger affinity between $Ca^{2+}$ ions and the PMEP functional

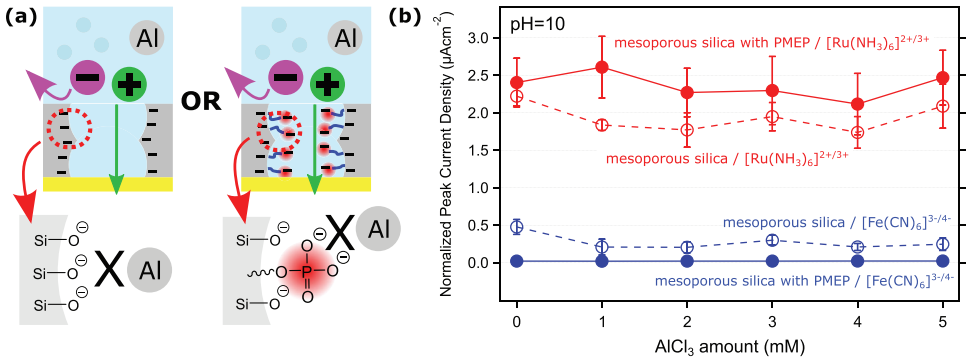


**Figure 5.** a) Illustration of Al species (filled grey circles) including electrolyte in contact with mesoporous silica pores without (left) and with PMEP functional pores (right) where the anionic ($[Fe(CN)_6]^{3-/4-}$, filled purple circle), and cationic ($[Ru(NH_3)_6]^{2+/3+}$, filled green circle) redox probes can or cannot access. b) Normalized peak current density ($i_{p,a}$) at different $Al^{3+}$ ion loadings obtained from the CV measurements of the transport of anionic (blue markers and left axis) and cationic probes (red markers and right axes) through the non-functional (empty circles) and PMEP filled (filled circles) pores at pH = 10. Error bars are sd.

pores compared to those at non-functional pores. Langmuir binding constants in both PMEP functionalized and unfunctionalized mesoporous films also revealed that $Ca^{2+}$ ion adsorption has a stronger impact on the transport of anionic probes than the cationic probe transport. Thus, in alkaline conditions, $Ca^{2+}$ ion binding could regulate the cation nanopore transport only inside the PMEP-functional pores due to their high $Ca^{2+}$ ion affinity. However, $Ca^{2+}$ ion-binding inside the lower affinity non-functional pores cannot regulate cation transport. Besides tuning the ionic transport gradually, the stronger $Ca^{2+}$ ion-binding at the PMEP functional mesopores also has a direct role in both i) adsorption/desorption (reversibility) mechanism of $Ca^{2+}$ ions and ii) $Ca^{2+}$ ion detection sensitivity (160 μA $cm^{-2}$ μM) at sub-μM (500 nM) concentrations. Compared to the PMEP-functional pores, our non-functional silica pores showed $Ca^{2+}$ adsorption/desorption reversibility even at basic pH but limited $Ca^{2+}$ ion detection sensitivity via presenting a lower increase in the peak current density after $Ca^{2+}$ addition (40 μA $cm^{-2}$ μM after 500 nM $Ca^{2+}$ ion addition). This is so though higher sensitivity (160 μA$cm^{-2}$ $μM^{-1}$ after 500 nM $Ca^{2+}$ ion addition) to the $Ca^{2+}$ presence in PMEP-functional pores causes a limited capability to release the attached $Ca^{2+}$ ions. Still, we demonstrated that lowering the pH of the electrolyte could be used to partly release the $Ca^{2+}$ ions from these PMEP-functional pores via neutralizing the deprotonated phosphate groups, indicating a strong memory effect of PMEP polyelectrolyte functionalized pores under the applied conditions. In the end, we also showed that our nanopore systems are only sensitive to binding $Ca^{2+}$ ions to themselves but not the multivalent Al ionic species.

## 4. Experimental Section

*Chemicals*: Ethanol (absolute EMPLURA), Pluronic F127, 2-(methacryloyloxy)ethyl phosphate (MEP, 90%), tetraethylorthosilicate (TEOS) (98%, reagent grade), $CaCl_2$ (anhydrous, granular, ≥93.0%), and $AlCl_3$ (ReagentPlus, 99%) had been purchased from Sigma–Aldrich/Merck. Toluene (anhydrous, 99.8%) was purchased from Alfa Aesar. All materials and solvents were used as received.

*Mesoporous Silica Thin Film Preparation*: Mesoporous silica thin films were prepared by the sol–gel process using tetraethylorthosilicate (TEOS) as the inorganic precursor and Pluronic F127 as the template. For the dip-coat solution, the following molar ratio was used and mixed in the listed order: 40 ethanol: 1 TEOS : 0.0075 F127: 10 $H_2O$: 0.28 HCl (37%). The solution was stirred overnight and stored at −18 °C when it was unused. The mesoporous silica thin films were coated on glass substrates (microscopy slides, VWR), glass substrates with an indium tin oxide layer on the top (ITO, Delta Technologies, 4–8 Ω), and silicon wafers (Si-Mat, Kaufering, Germany, 100 mm diameter, 525 ± 25 μm thickness, type P/Bor, <100> orientation, CZ growth method, 2–5 W resistivity, polished on one side). The substrates were dip-coated at 50% relative humidity (RH) and at 25 °C by using the previously reported evaporation-induced self-assembly method (EISA-process).[28] The substrate surfaces were wiped using a fabric soaked with ethanol before the dip-coating. Afterward, the substrates were dip-coated with a 120 mm min withdrawal speed. The deposited films were kept under the same climate conditions for at least 1 h before calcination. The films were calcinated by following heating sequence: heating up to 60 °C in 10 min, holding the temperature at 60 °C for 1 h, a temperature increase to 130 °C within 10 min, and holding the temperature at 130 °C for 60 min; subsequently, the temperature was increased to 350 °C using a heating rate of 1 °C $min^{-1}$ and the temperature was kept constant at 350 °C for 2 h. As the final step of the calcination, the temperature program ended, and the samples were taken out after the oven reached room temperature (≈25 °C).

*Grafting of N,N-(diethylamino)dithiocarbamoylbenzyl (trimethoxy) silane) (SBDC) in Mesopores*: The synthesis of the iniferter *N,N*-(diethylamino)dithiocarbamoylbenzyl (trimethoxy)silane) (SBDC) was performed according to previous literature protocol.[29] First, 14.4 mg SBDC was solved in 40 mL (34.7 g) dry toluene under an inert gas atmosphere. The solution was then flushed with nitrogen for 10 min before being transferred to a separate dry Schlenk flask containing the mesoporous film coated substrates. The Schlenk tube was placed in a water bath (80 °C) for 1 h. After that, the substrates were washed with toluene. After SBDC grafting, the films were $CO_2$-plasma treated to remove the iniferter at the outer planar surface as described by Krohm et al.[42] and Babu et al.[43] using a Diener Electronic 20 Femto plasma system. The pressure was 0.3 mbar with a power of 20% (10 watts) for 12 s.

*PMEP Modification of the Silica Mesopores*: The PMEP modification of the silica mesopores was performed by an iniferter-initiated photopolymerization by using UV-Light (365 nm). 0.55 g MEP was dissolved in 14 mL distilled water and flushed with nitrogen for 10 min. Afterward, the SBDC functionalized silica films were placed in the solution under an inert gas atmosphere and were irradiated using a Bio-Link BLX by Vilber Lourmat for 10 min ($\lambda$ = 365 nm, $P$ = 40 W). After irradiation, the films were washed and extracted in distilled water overnight.

*Attenuated Total Reflection Fourier Transform Infrared Spectroscopy (ATR-FTIR)*: Attenuated total reflection IR (ATR-IR) measurements were performed by using a Spectrum One Fourier transform infrared (FT-IR) spectrometer from PerkinElmer. The silica films were scratched off the substrates using a razor blade and left on the top of the ATR-IR crystal for the measurements. ATR-IR spectra were collected in the range from 650 to 4000 $cm^{-1}$, and each spectrum was background-corrected using the device software's background correction tool. In addition, the IR-spectra were baseline corrected and normalized to the Si—O—Si asymmetric stretching vibrational band at ≈1060 $cm^{-1}$ by using OriginPro9.

*Ellipsometry*: Ellipsometry measurements were used to determine the refractive indices and film thicknesses of the mesoporous silica thin films on silicon wafers using the nanofilm EP3-SE from the company ACCURION with a 658 nm laser. The software EP4-View and EP4-model (version 1.2.0) were used for measurements and model analysis. The angle of incidence (AOI) was varied from 38° to 68° in 2° increments and measured in one-zone mode (Si-wafer → $SiO_2$-oxide layer → $SiO_2$ mesoporous) at a relative humidity of 15% to exclude water condensation inside the mesopores. The program Regul'Hum (version 3.3) was used to control the relative humidity. The free pore volume calculation was carried out using the refractive indices according to Brüggemann's effective medium theory described in the literature.[44,45]

*Cyclic Voltammetry, Peak Current Density Quantification*: Cyclic voltammetry measurements were performed by using an Autolab PGSTAT302N potentiostat from Metrohm Autolab BV operated by a software called Nova 2.0. The pore transport was analyzed by using electrolytes consisting of 100 mM of KCl and 1 mM of $[Fe(CN)_6]^{3-/4-}$ or 1 mM of $[Ru(NH_3)_6]^{2+/3+}$ as negatively- or positively charged probe molecules, respectively. In addition, to study ligand-binding triggered nanopore transport, electrolytes were loaded with different concentrations of $Ca^{2+}$ or $Al^{3+}$ ions by adding different amounts of $CaCl_2$ to the electrolyte solutions. As the first step of cyclic voltammetry measurements at changing the $Ca^{2+}$ amount (binding), several CV curves were collected by using the identical electrolyte without $Ca^{2+}$ inside ($Ca^{2+}$ = 0 mM) at increasing electrolyte–mesoporous film interaction times (Figure S3, Supporting Information). This was done to monitor changes in the CV curves based on the nanopore–electrolyte interaction time, such as pore opening (stabilization) and to avoid these changes to interpret the results. After reaching such a plateau, the CV from other electrolytes with higher amounts of $Ca^{2+}$ ions inside started to be collected at the same measurement position. To avoid the time-dependent pore activation effect (as the factor of

increasing film-electrolyte interaction time) for each $Ca^{2+}$ concentration measurement, the anodic current peak density, $i_{p,a}$ (Figure S13, Supporting Information),[37] after the current density reached a plateau, was saved as done for measuring the $Ca^{2+}$ = 0 mM electrolyte. The pH values were set using diluted hydrochloric acid or sodium hydroxide solution. For cyclic voltammetry measurements, a three-electrode system was used: Ag/AgCl electrode (BASi, Typ RE-6) as reference electrode, graphite electrode (Alfa Aeasar) as the counter electrode, and the ITO layer of the silica-coated substrate (Delta Technologies, 4–8 Ω) as the working electrode. Before each cyclic voltammetry measurement, the samples were incubated in 100 mM KCl solution for at least 1 h. The contact area (opening) between the electrolyte and the measured mesoporous film was 0.21 $cm^2$. Each condition was measured at least once using a scan rate sequence of 200, 100, 25, 300, 500, and 200 mV $s^{-1}$, while each scan rate cycled three times. For evaluation, the scan rate of 200 $mVs^{-1}$ was used. To generate peak current density versus $CaCl_2$ amount plots (Figure 3, Figure S7, Supporting Information), first, the absolute (non-normalized) peak current densities were collected from the anodic ($i_{p,a}$) (as well as cathodic, $i_{p,c}$; see Figure S7c,d; Supporting Information) portion of each CV curve presented in Figure 2; Figure S4, Supporting Information. $i_{p,a}$ and $i_{p,c}$ were quantified from the peaks in oxidation and reduction part, respectively, after defining a proper baseline correction as explained in the literature (Figure S13, Supporting Information).[37]

*Normalization of the Peak Current Density ($i_{p,a}$ and $i_{p,c}$) Data*: Even after using identical dip-coating protocols, sometimes mesoporous films result in a slight (non-significant) difference in their thickness and free pore volume (Figure S8, Supporting Information). Thus, the ionic transport at these films presented an offset in their peak current densities at different $Ca^{2+}$ ion filling levels (Figure S8a, Supporting Information). Such offset was eliminated by normalizing the entire data from CV measurements. Every peak current density obtained from CV measurements of anionic (Equation (1)) or cationic (Equation (2)) redox probes at different $Ca^{2+}$ loadings was normalized to the peak current density of these probes measured at pH = 3 environment, and when there was no $Ca^{2+}$ ion (0 mM) in the electrolyte. Mathematical descriptions of the normalization method are also shown below,

$$i^{\left[Fe(CN)_6\right]^{3-/4-}}_{p,a,\,normalized} = \frac{\left[i^{\left[Fe(CN)_6\right]^{3-/4-}}_{p,a}\left(Ca^{2+} = 0\ \text{mM}\ or\ 0.125\ \text{mM}\ or\ \cdots\right) at\ (pH = 10)\ or\ (pH = 3)\right]}{i^{\left[Fe(CN)_6\right]^{3-/4-}}_{p,a}\left(Ca^{2+} = 0\ \text{mM}\right) and\ (pH = 3)} \quad (1)$$

$$i^{\left[Ru((NH_3)_6\right]^{2+/3+}}_{p,a,\,normalized} = \frac{\left[i^{\left[Ru((NH_3)_6\right]^{2+/3+}}_{p,a}\left(Ca^{2+} = 0\ \text{mM}\ or\ 0.125\ \text{mM}\ or\ \cdots\right) at\ (pH = 10)\ \ or\ (pH = 3)\right]}{i^{\left[Ru((NH_3)_6\right]^{2+/3+}}_{p,a}\left(Ca^{2+} = 0\ \text{mM}\right) and\ (pH = 3)} \quad (2)$$

The reason for using the peak current density from CV measurements of electrolytes whose pH = 3 and includes no $Ca^{2+}$ ion inside is that at these conditions, the pores are neutral, and there is no $Ca^{2+}$ and pore wall interaction possibility. At pH = 3 and 0 mM $Ca^{2+}$ conditions (Figure S4, Supporting Information), no significant change in the transport of anions and cations was detected when the absolute (non-normalized) peak current densities of ions at these neutral pores were compared.

*Langmuir Adsorption Isotherm Fittings to the Experimental CV Results*: At high $Ca^{2+}$ ion and charged nanopore wall (at pH = 10) interactions in both PMEP functional and non-functional systems, the peak current densities (normalized and absolute) reached a plateau (Figure 3a,b). Therefore, it is concluded that the higher anionic probe transport at negatively charged pores upon more prominent $Ca^{2+}$ ion addition is the consequence of increasing $Ca^{2+}$ ion adsorption to these pores. To study this relation, it was described by using Langmuir isotherms (Equation (3)):[46]

$$i_p = i_{p,0} + i_{p,sat}\left(\frac{bC}{1+bC}\right) \quad (3)$$

where $i_p$ is the peak current density at a specific concentration ($C$) of $CaCl_2$ inside the electrolyte. $i_{p,0}$ is the peak current density measured at 0 mM $CaCl_2$, $i_{p,sat}$ is the peak current density value where the $Ca^{2+}$ ion adsorption saturates were saved at increasing amounts of $CaCl_2$ between 0 and 5 mM. b is the Langmuir adsorption constant (dissociation constant) describing the affinity of $Ca^{2+}$ ions to the binding sites at the pores.

*Incubation of Films in Electrolytes and Their SEM Imaging*: Before the incubation tests, the PMEP-functional mesoporous films were left inside KCl solution (100 mM) for 1 h. Subsequently, the films were incubated inside electrolytes, including 100 mM KCl, 1 mM $[Fe(CN)_6]^{3-/4-}$ and having pH of 3 or 10 for 370 and 200 min, respectively. The films' stability after incubation was tested by checking the free pore volume and thickness change of the films before and after incubation by Ellipsometry (see above).

For the SEM imaging, the PMEP-functional silica mesoporous before and after incubation was fixed on sample holders by using conducting and double-side adhesive carbon-based tapes. Afterward, the samples were coated with a 7 nm platinum/palladium layer using a Cressington 208 HR Sputter Coater. The SEM measurements were performed on Zeiss EVO 10 with the software SmartSEM at 30 kV of acceleration voltage and using a secondary electron as the detector at a working distance of ≈7 mm.

## Supporting Information

Supporting Information is available from the Wiley Online Library or from the author.

## Acknowledgements

The authors acknowledge funding from the ERC: European Research Council (ERC) under the European Union's Horizon 2020 research and innovation program (grant agreement No 803758). H.S.V thankfully acknowledges funding from the Career Bridging Grant (CBG_10_JUNI_2021_Varol) given by the Technische Universität Darmstadt (TU-Darmstadt). The authors thank Ulrike Kunz from the Materials Science Department at TU-Darmstadt for the help with the TEM imaging of the mesoporous film. The authors want to especially thank Dr. Robert Brilmayer (BASF, Germany), Dr. Mathias Stanzel, and Dr. Adnan Khalil (TU-Darmstadt) for the fruitful discussion and insight regarding CV data and their interpretations.

## Conflict of Interest

The authors declare no conflict of interest.

## Data Availability Statement

The data that support the findings of this study are available from the corresponding author upon reasonable request.

## Keywords

calcium binding, ion transport, mesoporous silica thin films, polyelectrolytes, sensing

Received: August 28, 2022
Revised: November 22, 2022
Published online: February 2, 2023

[1] D. C. Malaspina, G. Longo, I. Szleifer, *PLoS One* **2017**, *12*, e0185518.
[2] Y. Li, Y. Xiong, D. Wang, X. Li, Z. Chen, C. Wang, H. Qin, J. Liu, B. Chang, G. Qing, *NPG Asia Mater.* **2019**, *11*, 46.
[3] A. Picones, J. I. Korenbrot, *Biophys. J.* **1995**, *69*, 120.
[4] J. Xue, Y. Han, W. Zeng, Y. Wang, Y. Jiang, *Neuron* **2021**, *109*, 1302.
[5] M. Ali, S. Nasir, P. Ramirez, J. Cervera, S. Mafe, W. Ensinger, *ACS Nano* **2012**, *6*, 9247.
[6] A. Brunsen, C. Díaz, L. I. Pietrasanta, B. Yameen, M. Ceolín, G. J. A. A. Soler-Illia, O. Azzaroni, *Langmuir* **2012**, *28*, 3583.
[7] R. Brilmayer, C. Hess, A. Andrieu-Brunsen, *Small* **2019**, *15*, 1902710.
[8] S. J. Lounder, A. Asatekin, *Proc. Natl. Acad. Sci. USA* **2021**, *118*, e2022198118.
[9] R. Epsztein, R. M. Duchanois, C. L. Ritt, A. Noy, M. Elimelech, *Nat. Nanotechnol.* **2020**, *15*, 426.
[10] A. Soozanipour, H. Sohrabi, F. Abazar, A. Khataee, A. Noorbakhsh, M. Asadnia, A. Taheri-Kafrani, M. R. Majidi, A. Razmjou, *Adv. Mater. Technol.* **2021**, *6*, 2000765.
[11] M. Li, Y. Cao, X. Zhang, D. Wang, S. Qian, G. Li, F. Zhang, Y. Xiong, G. Qing, *Chem. Commun.* **2021**, *57*, 7914.
[12] R. Pardehkhorram, A. Andrieu-Brunsen, *Chem. Commun.* **2022**, *58*, 5188.
[13] Y. A. Perez Sirkin, M. Tagliazucchi, I. Szleifer, *Mater. Today Adv.* **2020**, *5*, 100047.
[14] O. Schepelina, I. Zharov, *Langmuir* **2006**, *22*, 10523.
[15] B. Yameen, M. Ali, R. Neumann, W. Ensinger, W. Knoll, O. Azzaroni, *J. Am. Chem. Soc.* **2009**, *131*, 2070.
[16] B. Yameen, M. Ali, R. Neumann, W. Ensinger, W. Knoll, O. Azzaroni, *Nano Lett.* **2009**, *9*, 2788.
[17] J. Elbert, F. Krohm, C. Rüttiger, S. Kienle, H. Didzoleit, B. N. Balzer, T. Hugel, B. Stühn, M. Gallei, A. Brunsen, *Adv. Funct. Mater.* **2014**, *24*, 1591.
[18] T. Ma, J. Janot, S. Balme, *Small Methods* **2020**, *4*, 2000366.
[19] R. Brilmayer, S. Kübelbeck, A. Khalil, M. Brodrecht, U. Kunz, H. Kleebe, G. Buntkowsky, G. Baier, A. Andrieu-Brunsen, *Adv. Mater. Interfaces* **2020**, *7*, 1901914.
[20] J.-G. Wu, S.-C. Wei, S.-C. Luo, J.-G. S. Wu, -C. Luo, -C. S. Wei, *Adv. Mater. Interfaces* **2020**, *7*, 2000470.
[21] A. Khalil, M. Zimmermann, A. K. Bell, U. Kunz, S. Hardt, H. J. Kleebe, R. W. Stark, P. Stephan, A. Andrieu-Brunsen, *J. Colloid Interface Sci.* **2020**, *560*, 369.
[22] G. Pérez-Mitta, A. G. Albesa, C. Trautmann, M. E. Toimil-Molares, O. Azzaroni, *Chem. Sci.* **2017**, *8*, 890.
[23] A. Andrieu-Brunsen, S. Micoureau, M. Tagliazucchi, I. Szleifer, O. Azzaroni, G. J. A. A. Soler-Illia, *Chem. Mater.* **2015**, *27*, 808.
[24] V. Motta, M. Schäfer, J. Hühn, R. Zierold, R. H. Blick, W. J. Parak, K.-M. Weitzel, V. Motta, M. Schäfer, K.-M. Weitzel, J. Hühn, R. Zierold, R. H. Blick, W. J. Parak, *Adv. Mater. Interfaces* **2020**, *7*, 2000419.
[25] E. G. Solveyra, R. J. Nap, K. Huang, I. Szleifer, *Polymers* **2020**, *12*, 2282.
[26] M. Tagliazucchi, I. Szleifer, *Mater. Today* **2015**, *18*, 131.
[27] L. G. Lopez, R. J. Nap, *Phys. Chem. Chem. Phys.* **2018**, *20*, 16657.
[28] C. J. Brinker, Y. Lu, A. Sellinger, H. Fan, *Adv. Mater.* **1999**, *11*, 579.
[29] J. C. Tom, R. Brilmayer, J. Schmidt, A. Andrieu-Brunsen, *Polymers* **2017**, *9*, 539.
[30] L. Silies, H. Didzoleit, C. Hess, B. Stühn, A. Andrieu-Brunsen, *Chem. Mater.* **2015**, *27*, 1971.
[31] M. Stanzel, R. Brilmayer, M. Langhans, T. Meckel, A. Andrieu-Brunsen, *Microporous Mesoporous Mater.* **2019**, *282*, 29.
[32] F. M. Gilles, M. Tagliazucchi, O. Azzaroni, I. Szleifer, *J. Phys. Chem. C* **2016**, *120*, 4789.
[33] E. Piccinini, C. Bliem, J. M. Giussi, W. Knoll, O. Azzaroni, *Langmuir* **2019**, *35*, 8038.
[34] N. Herzog, H. Hu, C. Ru, M. Gallei, A. Andrieu-Brunsen, *Langmuir* **2020**, *36*, 4015.
[35] L. Silies, A. Andrieu-Brunsen, *Langmuir* **2018**, *34*, 807.
[36] P. Y. Steinberg, F. M. Zanotto, G. J. A. A. Soler-Illia, S. A. Dassie, P. C. Angelomé, *J. Phys. Chem. C* **2021**, *125*, 23521.
[37] N. Elgrishi, K. J. Rountree, B. D. McCarthy, E. S. Rountree, T. T. Eisenhart, J. L. Dempsey, *J. Chem. Educ.* **2018**, *95*, 197.
[38] B. A. Legg, M. D. Baer, J. Chun, G. K. Schenter, S. Huang, Y. Zhang, Y. Min, C. J. Mundy, J. J. De Yoreo, *J. Am. Chem. Soc.* **2020**, *142*, 6093.
[39] P. Ramirez, J. A. Manzanares, J. Cervera, V. Gomez, M. Ali, I. Pause, W. Ensinger, S. Mafe, *J. Membr. Sci.* **2018**, *563*, 633.
[40] B. Sun, X. G. Hao, Z. De Wang, G. Q. Guan, Z. L. Zhang, Y. Bin Li, S. Bin Liu, *J. Hazard. Mater.* **2012**, *233*, 177.
[41] X. Du, X. Sun, H. Zhang, Z. Wang, X. Hao, G. Guan, A. Abudula, *Electrochim. Acta* **2015**, *176*, 1313.
[42] F. Krohm, J. Kind, R. Savka, M. Alcaraz Janßen, D. Herold, H. Plenio, C. M. Thiele, A. Andrieu-Brunsen, *J. Mater. Chem. C* **2016**, *4*, 4067.
[43] D. J. Babu, S. Yadav, T. Heinlein, G. Cherkashinin, J. J. Schneider, *J. Phys. Chem. C* **2014**, *118*, 12028.
[44] C. Boissiere, D. Grosso, S. Lepoutre, L. Nicole, A. B. Bruneau, C. Sanchez, *Langmuir* **2005**, *21*, 12362.
[45] A. Brunsen, A. Calvo, F. J. Williams, G. J. A. A. Soler-Illia, O. Azzaroni, *Langmuir* **2011**, *27*, 4328.
[46] R. H. Tunuguntla, F. I. Allen, K. Kim, A. Belliveau, A. Noy, *Nat. Nanotechnol.* **2016**, *11*, 639.